Well Plate Integrated Topography Gradient Screening Technology for Studying Cell-Surface Topography Interactions

van der Boon, Torben A. B.; Yang, Liangliang; Li, Linfeng; Calvan, Daniel E. Cordova; Zhou, Qihui; de Boer, Jan; van Rijn, Patrick

Published in:
Advanced biosystems

DOI:
10.1002/adbi.201900218

Publication date:
2020

ADVANCED BIOSYSTEMS
www.adv-biosys.com

Well Plate Integrated Topography Gradient Screening Technology for Studying Cell-Surface Topography Interactions

*Torben A. B. van der Boon, Liangliang Yang, Linfeng Li, Daniel E. Córdova Galván, Qihui Zhou, Jan de Boer, and Patrick van Rijn**

New high-throughput technologies for cell–material interaction studies provide researchers with powerful tools to speed up research in the field of biomaterial–cell interactions. However, sharing technologies is often difficult due to the necessity of specific knowledge and experiences. Engineered surfaces can elucidate effects of surface topography on cell behavior, which is of critical value for gaining control over cellular processes. Here, the translation of a gradient-based high-throughput cell screening approach for aligned nano/ micro topographies interacting with cells is presented. An aligned topography 96-well plate is created by upscaling of highly specific gradient technology. The resulting cell culture dishes are compatible with general laboratory and imaging equipment, and the platform allows for studying cell behavior with regard to adhesion and alignment. The challenge lies in increasing the dimensions of the previous 1 × 1 cm gradient topography substrate, to be able to cover the span of a 96-well plate and translate it into a standardized cell-screening tool. Adhesion experiments of human bone marrow derived mesenchymal stem cells confirm the standardization, compatibility, and usability of the technology. In the process of using multi-system imaging and analysis, it becomes apparent that future challenges need to include universally applied data analysis approaches.

1. Introduction

In current medicine, biomaterials are indispensable and used more and more often in patient treatment with respect to lifestyle assisting, or medical implantation devices. The materials used in these applications directly come in contact with human tissues and the cells within. It is well-known that the human body, its tissues, and cells react to these biomaterials,[1–3] and upon implantation, the materials trigger an altered cellular behavior such as a foreign body response.[4–7] As a result, in ongoing research, the trend is shifting to developing more bio-instructive[8,9] instead of bio-inert materials. Cells have been found to respond to material parameters, such as the material's chemistry, stiffness, and topography.[10–20] The chemistry and wettability of a surface together dictate the adsorbance of proteins to the surface, which influences cell adhesion.[19,21,22] Identifying how such material parameters influence cellular behavior is of crucial importance and can aid us in, for instance, implant technology development. A step in this direction is the development of "smart biomaterials."[23,24] These developments will ultimately improve treatment of disease and add to patient comfort. Elucidating the biomaterial's effect on cellular adhesion, spreading, migration, proliferation, and differentiation is proving to be of unmistakable importance.[6,25] The insights gained from studying this delicate interface between the human tissues and medical implants will improve biomaterials and implant design, by optimizing their surface characteristics, resulting in a desired host response. For instance, the

T. A. B. van der Boon, L. Yang, D. E. Córdova Galván, Dr. Q. Zhou, Dr. P. van Rijn
W.J. Kolff Institute for Biomedical Engineering and Materials Science
Department of Biomedical Engineering
University Medical Center Groningen
University of Groningen
A. Deusinglaan 1, 9713 AV, Groningen, the Netherlands
E-mail: p.van.rijn@umcg.nl

The ORCID identification number(s) for the author(s) of this article can be found under https://doi.org/10.1002/adbi.201900218.

DOI: 10.1002/adbi.201900218

L. Li
Merln Institue for Technology-inspired Regenerative Medicine
Maastricht University
Universiteitssingel 40, 6229 ER, Maastricht, the Netherlands

Dr. Q. Zhou
Institute for Translational Medicine
State Key Laboratory of Bio-fibers and Eco-textiles
Qingdao University
Qingdao 266021, China

Prof. J. de Boer
Department of Biomedical Engineering
Eindhoven University of Technology
De Zaale, 5600 MB, Eindhoven, the Netherlands

transduction of material physical cues into intracellular biochemical information can result in activation of the integrin focal adhesion cytoskeleton actin transduction pathway, also known as "mechanosensing" and "mechanotransduction."[26,27] Signaling cascades associated with this morphology deformation can alter gene expression to regulate cell functions and promote tissue regeneration.[28] Engineering of biomaterials in such a manner often results in cell phenotypical changes, such as alignment and morphology, but also affects proliferation and cell migration.[29–31] Such an interdependent relationship between biomaterials and biology is proposed to be encompassed under the recently introduced concept of "materiobiology": "a scientific discipline that studies the biological effects of inherent properties of biomaterials on biological functions at cell, tissue, and whole organism levels."[2] As mentioned, cell behavioral response to these properties is widely studied, but most attempts only tackle a few distinct situations in a low-throughput fashion.[32–38] However, we, among others, already take a leap forward by making use of arrays or gradients,[18,39–50] or having developed screening platforms for bioactive surface topographies.[51,52] Such novel approaches provide researchers with more information in fewer experiments in a (semi)automated fashion, better known as high-throughput cell screening. Such high-throughput cell screening platforms are currently on the rise and prove to be the more efficient and cheaper alternative to conventional research methodology. Among others,[53,54] the TopoChip[55] is another example of a successful attempt to combine novel technologies with conventional research methods. Such approaches take the lead in the overall translation of in-house developed technology to a platform for conventional use. Here, we describe the successful translation of our previously established topography gradient technology[40–42,56] to a standardized format by integration with a commercial 96-well plate. We aimed to do so to make our topography gradient technology accessible to others as: 1) a 96-well plate is compatible with many standardized equipment and analysis approaches while a gradient substrate itself is not; 2) a 96-well plate is known and used by everyone and does not require additional training or experience while a gradient does, as it is vital to always exactly know at which position on the gradient one is performing the analysis. Striving to integrate new technologies with standardized research methodology provides better accessibility of new technologies for others. More importantly, a gradient well plate offers key advantages over using single gradient substrates, including the prevention of cross-communication of cells between different parts of the gradient by means of secreted soluble factors, as the wells are separated from one another. Stimulation of cells by means of topography alters their behavior and hence could also affect secretion of soluble factor that can be sensed by cells on different locations on the gradient and altered behavior might then not be solely due to topography anymore. The integration into the well plate prevents this, as every area is isolated within a well and communications between wells is not possible. Additionally, as there are several rows, both replicas and controlled biochemical stimulation is possible on the same plate while with the conventional linear gradient, several samples would be required. Our gradient well plate technology, thus, allows for studying the combined effects of material properties in the context of drugs and/or biomolecules on cell behavior, in order to identify optimal conditions, which will eventually lead to specific target applications. The conventional gradient samples were re-engineered to facilitate proper integration within well plate technology, and compatibility with different microscopy setups confirmed the general usability of the gradient topography plate. In addition to the general imaging approaches, also the data analysis on different systems was tested and both approaches proved applicable, without altering the corresponding flow of data analysis. Our gradient well plates have thus proven to be broadly applicable with conventional analysis setups, providing us and others with a powerful tool for the ongoing quest of understanding the complicated interactions at the cell-to-biomaterial interface.

2. Results and Discussion

The translation of our gradient technology toward a more standardized format that is compatible with generic cell biological protocols, requires key adjustments to the system. In our previous studies,[41–43] the gradients were kept relatively small, as it would allow us to use only a limited number of cells and surface area to analyze. However, using a gradient also means that great care needs to be taken when working with a gradient as it is pivotal to be able to accurately identify where on the surface the analysis is performed, as a small deviation may result in misinterpretation as to what topography is being analyzed. In order to translate the gradient technology toward a standardized format, a 96-well plate integration strategy was chosen, similarly to our previously published approaches using a bottomless well plate.[57] Before successful integration into a 96-well plate, the former gradient of 1 × 1 cm needed to be upgraded in order to cover a large portion of the bottom of a bottomless 96-well plate. Additionally, the individual wells should be isolated, so devoid of any leakage, and the bottom needs to be transparent and thin enough to be compatible with conventional microscopy setups.

2.1. Gradient Upscaling

For enabling the integration of the topography gradient technology into a more generally accepted tool, such as a 96-well plate culture dish, it was pertinent to increase the gradient from the initial 1.0 × 1.0 cm to a 9.0 × 8.0 cm substrate (**Figure 1**), which more than covers the dimensions of conventional 96-well plate bottoms, leaving one row as a control group (Figure S1, Supporting Information). Since our topography gradient is not established by means of lithography approaches, it is not as straightforward as designing a new mold with expanded areas and prepare a base plate via imprint lithography. Upscaling of substrate dimensions while maintaining the correct features, without altering the basic preparation approach, requires careful substrate engineering and continuous verification of feature maintenance. Therefore, we gradually increased the gradient substrate dimensions first to 2.0 × 2.0 cm, as for this area the same stretching device could be used and only the mask dimensions were altered (Figure 1).

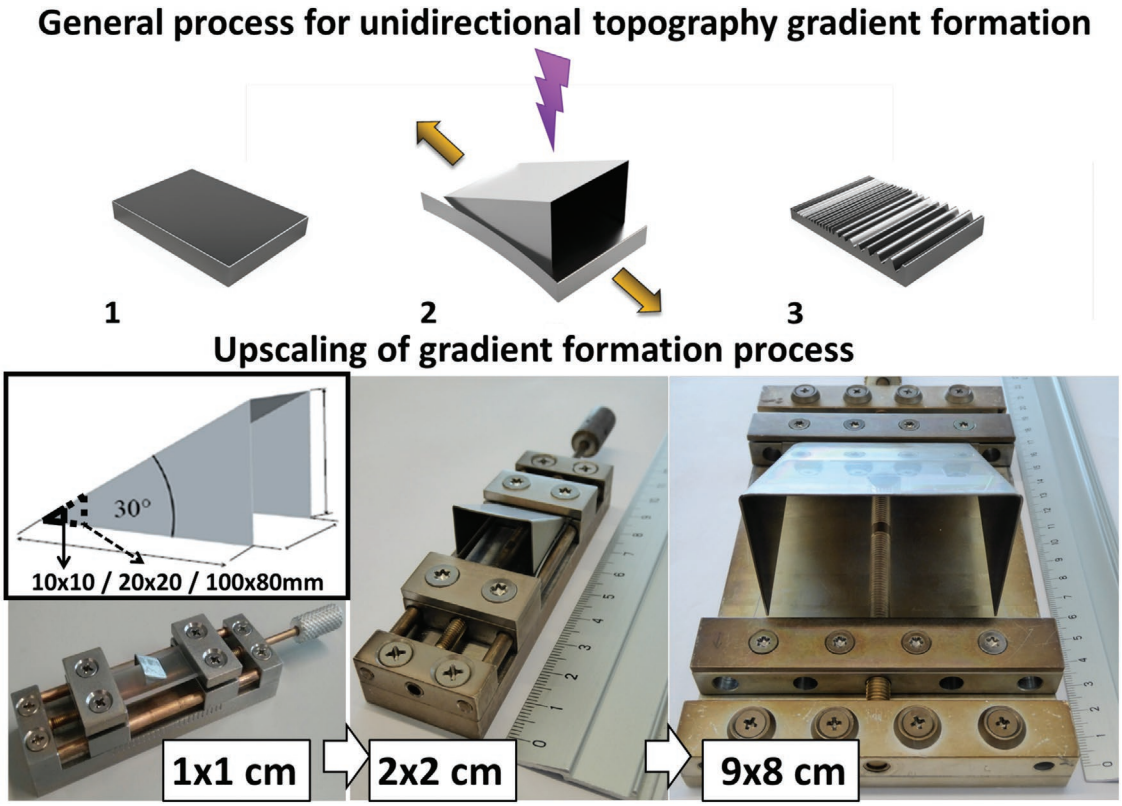

Figure 1. Basic approach for wrinkle topography preparation, in which the untreated sample (1) is stretched and oxidized (2), and wrinkles form upon release of strain (3). The mask ensures topography gradient formation by creating an oxidation gradient. For dimensional upscaling of the gradient substrate the PDMS substrate, mask, and stretching device were linearly increased in size.

After successful translation, the 9.0 × 8.0 cm approach was tested, which required both increased mask dimensions and enlargement of the stretching device (Figure 1). Initially the mask features were extended from 1.3 × 1.0 cm to 2.6 × 2.0 cm (L × W) that allowed the generation of a 2.0 × 2.0 cm gradient instead of a 1.0 × 1.0 cm gradient. During the topography preparation step, the substrate is stretched by 30%; this increase needs to be taken into account when specific final dimensions are targeted. The overall surface features that are produced via the stretch–oxidize–release method are aligned wave patterns that are visible by eye due to light diffraction (**Figure 2**). The amplitude and wavelength are coupled; larger wavelengths are associated with larger amplitudes and the feature sizes increase going from the closed side of the mask (most shielded) to the open side (least shielded), and extending to outside of the mask where the surface is fully exposed to plasma where the largest wrinkle dimensions are observed (Figure 2a). While altering plasma oxidation times would also accomplish a similar effect, due to the shielding, the effect is not exposure time but rather intensity of plasma exposure. The area outside of the mask is taken into account in the substrate production for creating the aligned topography well plate, as the topography features displayed on those areas are still highly relevant.

To have the gradient fit to the dimensions of a 96-well plate, a length of 9.5 cm was chosen (Figure S1, Supporting Information), to cover the plate, covering until column 11 half way. The features for the 1.0 × 1.0 cm gradient developed across the gradient vary from a wavelength (λ) of 1.4 μm and amplitude (A) 200 nm at 0 cm to λ: 14.2 μm and A: 4200 nm at the 1.0 cm position. The development is not a linear increase across the gradient but has a steeper increase toward the end of the gradient. By altering the mask dimensions, the 2.0 × 2.0 cm gradient substrate was produced and displayed the same surface features, namely aligned topography and within the same size range (Figure 2b). Although, the feature size development has a similar trend across the surface on both the 1.0 × 1.0 cm and the 2.0 × 2.0 cm gradient, the range on the 2.0 × 2.0 cm gradient is slightly narrower as compared to the 1.0 × 1.0 cm gradient. To elaborate on this, at the 0 cm position of the 2.0 × 2.0 cm gradient, λ: 1.4 μm and A: 80 nm was found indicating that the amplitude was decreased as compared to the 200 nm present on the 1.0 × 1.0 cm gradient. At the 2.0 × 2.0 cm end, λ: 13.4 μm and A: 2000 nm was found, a noticeable decrease in wave amplitude with respect to the topography features of the 1.0 × 1.0 cm gradient. This difference could be a consequence of increasing the mask but not adjusting the dimensions of the stretching device, the area covered and the way the plasma enters the masked area might be slightly variable due to the position of the mask with respect to the connection of the polydimethylsiloxane (PDMS) substrate that is clamped in the stretching device. For the 9.0 × 8.0 cm gradient substrate, both the mask and the stretching device were altered as the initial dimension of the stretching device was still appropriate for the 2.0 × 2.0 cm; for the 9.0 × 8.0 cm, it was too small. The delicate

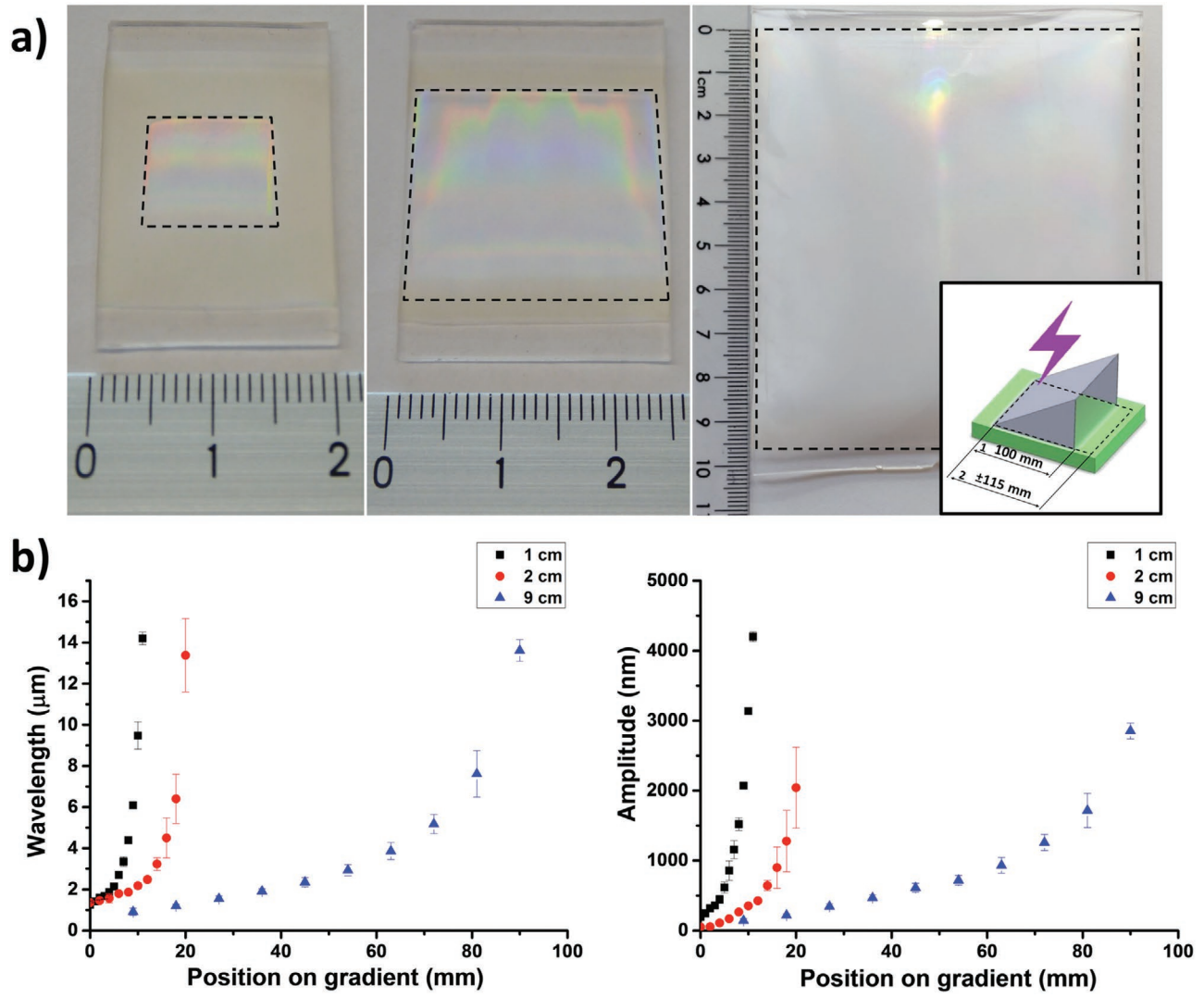

Figure 2. a) Photographs of the differently sized topography gradient substrates showing the distinct diffraction and below b) the development of the wavelength and amplitude of the topography along the gradient for the 1.0, 2.0, and 9.0 cm substrates ($N = 6$).

relationship between mask and stretching device dimensions were exemplified by the redesign as the displayed features on the 9.0 × 8.0 cm were in a similar size range as the 1.0 × 1.0 cm substrate. The mask used for creating a 9.0 × 8.0 cm substrate has the dimensions 10.0 × 8.0 cm. As shown in Figure 2, the starting λ and A were nearly the same; however, the final values at 10.0 cm (outside mask area) were λ: 14.0 µm and A: 2700 nm offering a lower amplitude than the 1.0 × 1.0 cm gradient, but higher than the 2.0 × 2.0 cm one. These findings indicate that upscaling in gradient technology is feasible, but still subject to alterations depending on the substrate size. The relationship between the stretching device, mask, and substrate size is a delicate one and indicates that upscaling and engineering approaches for translation of technology is not trivial. Although there are some variations between the differently sized gradients, the gradients themselves are highly reproducible and therefore suitable for the integration approach into established well plate technology.

2.2. Aligned Topography Well Plate Engineering

For integrating the newly expanded gradient substrate with the 96-well plate to create the aligned topography well plate, in the initial stage of the study, dimensions of 8.0 × 8.0 cm were chosen, which is obtained when a 10.0 × 8.0 cm mask is used for the preparation, using only the shielded area. This would allow for covering columns 1–8 across all the rows A–H. For covering a well, a 1 × 1 cm area is required. However, after analyzing the larger gradient substrate beyond the mask boundaries, as explained in the previous section, it was found that the gradient extends further and that columns 9 and 10 can be covered, still having distinctly different surface topography dimensions (**Figure 3**).

The gradient is joined together with a bottomless 96-well plate, whereby columns 1–10 and rows A–H are intended to study topography-driven cell response. Every row has the same development in topography, so 8 replicas are possible in total of 10 different topographies on a single well plate. As

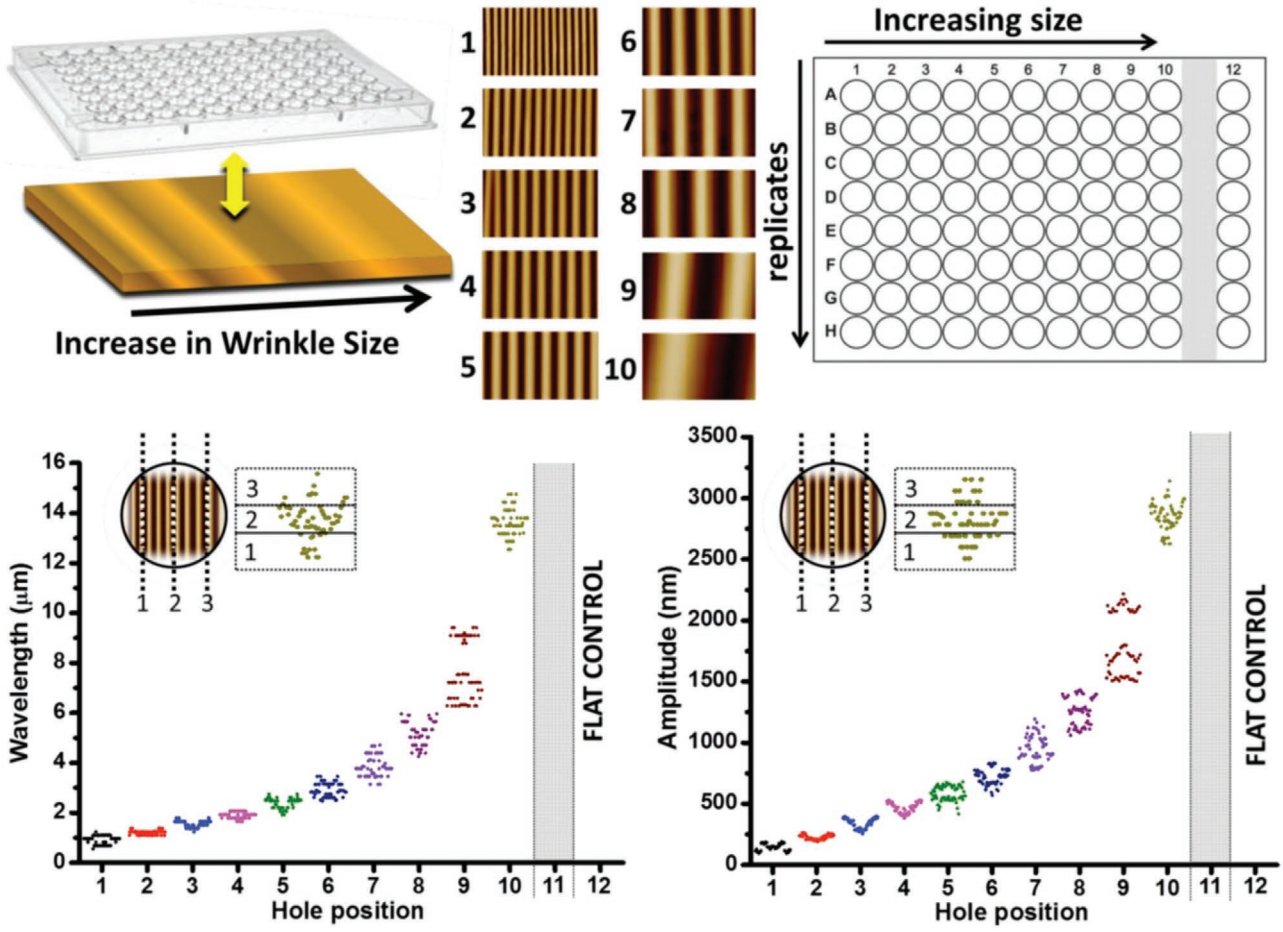

Figure 3. The topography gradient is integrated with 96-well plate technology and the well plate having 8 rows (A–H) and 12 columns (1–12) is covered completely until column 10 with the features while the last column (12) is covered with a planar control. Column 11 is a sacrificial column for the transition between gradient and control. Per well, the topography features have been determined and the wavelength and amplitude variation within a well is shown per column analyzed. Data was acquired from three different gradient samples ($N = 3$).

it is always desirable to have a planar control sample of the same material, a column for controls was added in column 12 leaving column 11 as a transition column that is not used for analysis. As this joining of two substrates may cause leakage, we chose to make the connection directly centered in column 11, which corresponds with a length of 9.5 cm (Figure S1, Supporting Information). For preventing inter-well communication and leakage, an extremely thin layer of liquid PDMS (Sylgard 184, 10:1 elastomer:cross-linker) is applied to the bottomless well plate (≈1.5 g per well plate) and placed in an oven at 70 °C for a quick initial ≈10 min curing step. This initial curing is necessary to prevent liquid PDMS to be pushed into the wells upon plate assembly and thereby covering substantial areas of topography. The topography gradient was placed together with the planar PDMS substrate, exactly across the well plate in a planar approach with mild and evenly applied pressure. The individual wells were visually inspected as it is easily observed when the substrate is not in good contact with the well plate. Subsequently, the aligned topography well plate was placed in an oven at 70 °C for 20 min with 4.5 kg of pressure evenly applied to it while curing. Finally, the bottom of the plate was sealed with 30 g of liquid PDMS evenly distributed to have a completely sealed bottom devoid of leakage. The plate was then cured for another 3 h at 70 °C.

Figure 3 displays the overall arrangement of the aligned topography well plate. The atomic force microscopy (AFM) images taken from the center of the wells at position in columns 1–10 illustrate the topography in the different columns. Every row is a replicate. It is important that integration of the topography gradient into the well plate does not affect the initially designed topography features or dimensions. Hence, the PDMS bottom was selectively removed from several wells after assembly and re-analyzed by AFM, which showed that, though few significant differences were found, these were not relevant as the average values are very similar and most likely originate from the chosen spots within the area as the area still presents a small gradient (Figure S2, Supporting Information).

2.3. Multi-System Imaging and Analysis

Applicability of the novel gradient topography well plate to different conventional imaging and analysis systems was assessed by imaging of human bone marrow derived mesenchymal

stem cells (hBM-MSCs) in a Nikon Eclipse Ti series inverted epifluorescence microscope, as well as in a Zeiss AxioImager. Z1 fluorescence inverted microscope controlled by TissueFAXS software (Tissue-Gnostics GmbH, Vienna, Austria), after which data was analyzed by CellProfiler and TissueQuest analysis software, respectively. The hBM-MSCs serve as a model cell type in this proof-of-concept study, since we have used these before with the initial gradient approach[42] and comparison in behavior is therefore possible. Also, hBM-MSCs are capable of differentiating into various lineages and aligned grated topography was previously used to study osteogenic differentiation[17,58] and therefore offers special interest for future studies with this cell type in our topography well plates. To ensure that topography is the only parameter that is influencing cellular behavior, all surfaces are post-treated with air plasma (as described in the method section) to obtain a homogenous full oxidation state omitting any deviations in chemical and mechanical surface properties. The oxidation also provides better support for cell culture compared to non-oxidized PDMS.

2.3.1. Imaging

Nikon Eclipse Ti: After mounting and calibrating the microscope with the gradient topography well plate, the software enabled a user-defined pattern of imaging; a total number of five images were taken per well in a random pattern inside the particular well. All wells containing the wrinkle pattern (A-H and 1–10), as well as the flat controls in column 12 were imaged. Using Nikon's NIS-Elements Viewer, the data acquired by the epifluorescence microscopy was made visible on screen, and CellProfiler software, a useful tool for cell analysis, allowed several cell features to be assessed. For cell staining, the Cell Painting[59] approach was used, and the cells were imaged and stored in different channels (1–4) containing, 1) nucleus, 2) ER/nucleoli, 3) Golgi/F-actin, 4) mitochondria. CellProfiler software allowed for assessment of these organelles in an independent manner.

TissueFAXS: Similar mounting and calibrating steps were taken in order for the gradient topography well plate to be imaged by the Zeiss microscope. Again, four main color channels were assigned to the fluorescent domains corresponding with aforementioned staining, allowing for independent analysis in TissueQuest and ImageJ software.

Overlay representation of images taken by both imaging systems are shown in **Figure 4**, comparing both data sets relative to their position on the wrinkle gradient (column in the gradient topography well plate). A trend in changing cell shape and orientation is very clearly made visible by both imaging systems, providing proof for general applicability as for which the system was designed for. This result as well as the way of using the well plate as any other well plate proves the successful translation of specialized gradient technology toward a general cell biological tool for investigating topography-driven cell behavior.

2.3.2. Data Analysis

As most imaging set-ups are coupled to their own means of data analysis, it is most convenient if a laboratory's flow of analysis is not hampered by the introduction of novel technologies. Therefore, it is crucial that the flow of analysis is kept according to the corresponding systems. To this end, we tested and found the gradient topography well plate to be applicable to both flows of data analysis, without the need to adjust either of the workflows.

Cell Orientation: Visual assessment of Figure 4 clearly reveals a change in cell shape and orientation as compared to their position on the wrinkle gradient. Data analysis in TissueQuest and ImageJ software support this statement, as the number of cells, which are completely aligned by the wrinkles, increased with wrinkle size (**Figure 5**). Cells were considered aligned when their major axis deviated less than 10 degrees (10<) from that of the wrinkles. A similar trend is observed in columns 1–7 when analyzing the data with CellProfiler software, whereas in columns 8–10, the distribution of aligned cells seems to broaden as compared to results from ImageJ analysis. A reason for this observed difference could possibly be found in differences in the software packages. A plausible explanation for this is the difference in determination of the cell's major axis between both analysis methods.

Determination of a cell's major and minor axis is significantly different in both analysis methods, as one relies on human assessment of the image, and the other on computer-based algorithms. In ImageJ analysis, major (and minor) axes are determined by the observer, allowing for direct adjustments during the measurements if needed. On the other hand, CellProfiler uses an algorithm to determine both axes. The parameters in this algorithm are set upfront by the user and will not change once the analysis is initiated. A drawback in this flow of analysis could be that when the quality among the images differs, due to difference in uptake of fluorescent dye for instance, or other experimental or imaging variations, the image quality might differ, and therefore the standards for detecting cell shape and axes could vary between the images. Such variations could be detected and adjusted for in a manual analysis by the human eye, constantly performing an image quality check per image. On the other hand, a pre-defined, computerized algorithm allows for thresholding beyond human perception, which might elucidate information in the image sets not detectable by the human eye. It is not at all a matter of trying to claim one method to be superior to the other, but it was made obviously clear to us that such variations in flow of analysis yield significant differences in outcome.

Cell Shape—Aspect Ratio: As is the case for the cell orientation, the aspect ratio of the cells is affected by the wrinkle gradient. Where cells were more randomly shaped and spread on the smaller wrinkles, specific elongated shapes were observed in the wells corresponding to the larger wrinkle sizes (Columns 6 through 10, Figure 4). This trend also shows a gradual, gradient-like change, as was the case for the wrinkle gradient itself and the cell orientation found previously using the smaller gradient samples.[42] Analysis in ImageJ (**Figure 6**a) clearly shows this increasing trend in elongation of the cells. On the other hand, data analysis using CellProfiler does not show the same trend and the determined aspect ratios were around the same value throughout the whole gradient, corresponding with similar values as observed in columns 1–6 in ImageJ analysis. Again, this difference may well be explained by the differences in analysis methods.

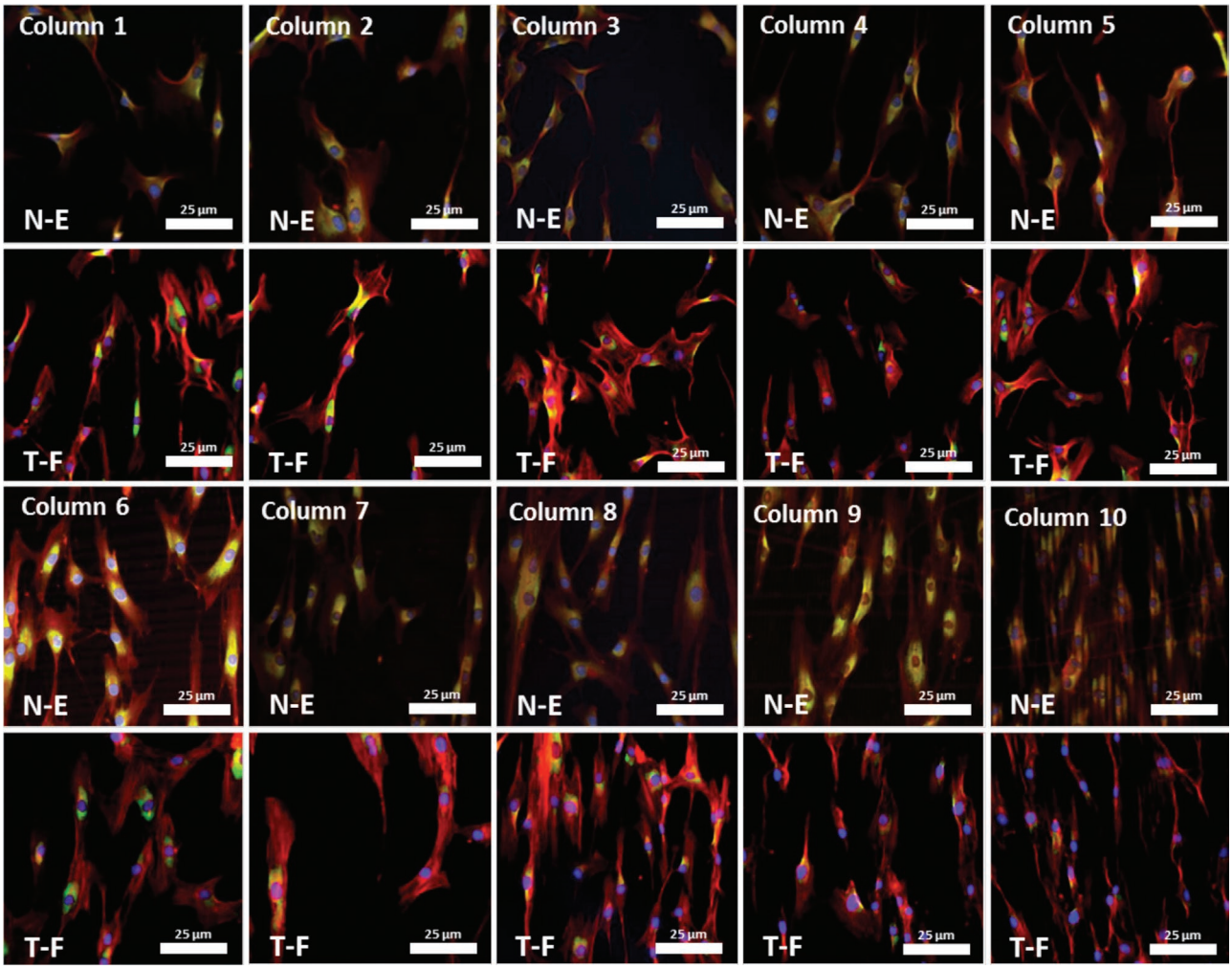

Figure 4. Overlay images taken by Nikon Eclipse TI (N-E) and TissueFAXS (T-F) microscopes. Shown are images per column, giving a comprehensive comparison between both imaging systems. Note that exactly the same plate with the same cells was used for both image sets. Larger scale images can be found in Figure S4, Supporting Information. Visualized cell compounds, using cell painting[59] staining technique are the nucleus (Hoechst: blue [447 nm]), endoplasmic reticulum (concanavalin A: green [520 nm]), nucleoli (SYTOa 14: red [593 nm]), Golgi apparatus and plasma membrane (WGA: red [642 nm]), F-actin (phalloidin: red [642 nm]), and mitochondria (MitoTracker: red [692 nm]).

For the aspect ratio, in both cases, the elongation is taken as the cell's major axis divided by its minor axis. As explained earlier, concerning both segmentation methods and axes determination, both methods differ from one another, yielding different results. CellProfiler artificially generates an ellipse shape around the identified objects. The length of the major axis of the cell is taken as the length of the major axis of the ellipse that has the same normalized second central moments as the region (object). In other words, an ellipse is drawn around an object (cell), which corresponds exactly with this object's normalized second central moments. The same method is applied in determining the minor axis length. On the one hand, the user adjustable analysis method might be more reliable in determining aspect ratio, as again image quality can be assessed per image and per measurement the actual cell shape is visually assessed. However, this method is more prone to observer bias, and the automated analysis is not. The latter, however, could be prone to misinterpretations of cell shape by the automated program, for instance, ellipses being determined by an extreme in cell shape, not representing the major body of the object, or for that matter, leaving out a certain part of the cell body. From our experience using the ellipse method, we have found the ellipses to usually have a slightly shorter major axis or longer minor axis, as compared to human observation, resulting in a reduction in aspect ratio. Next to this, as the manual axis determination differs from computerized shape recognition, this most probably adds to differences in distribution of aligned cells as seen in Figure 5. Both analysis methodologies have their advantages and disadvantages, but this also illustrates an important aspect related to material–cell interaction studies. In our pursuit for high-throughput cell screening and analysis, where we aim to particularly take care of preparing reproducible material properties and include rigorous material testing in order to get to the core of what interaction parameters are most influential, we are faced with the next eminent problem, namely, the data analysis approach that is not unified yet and yields variations in results.

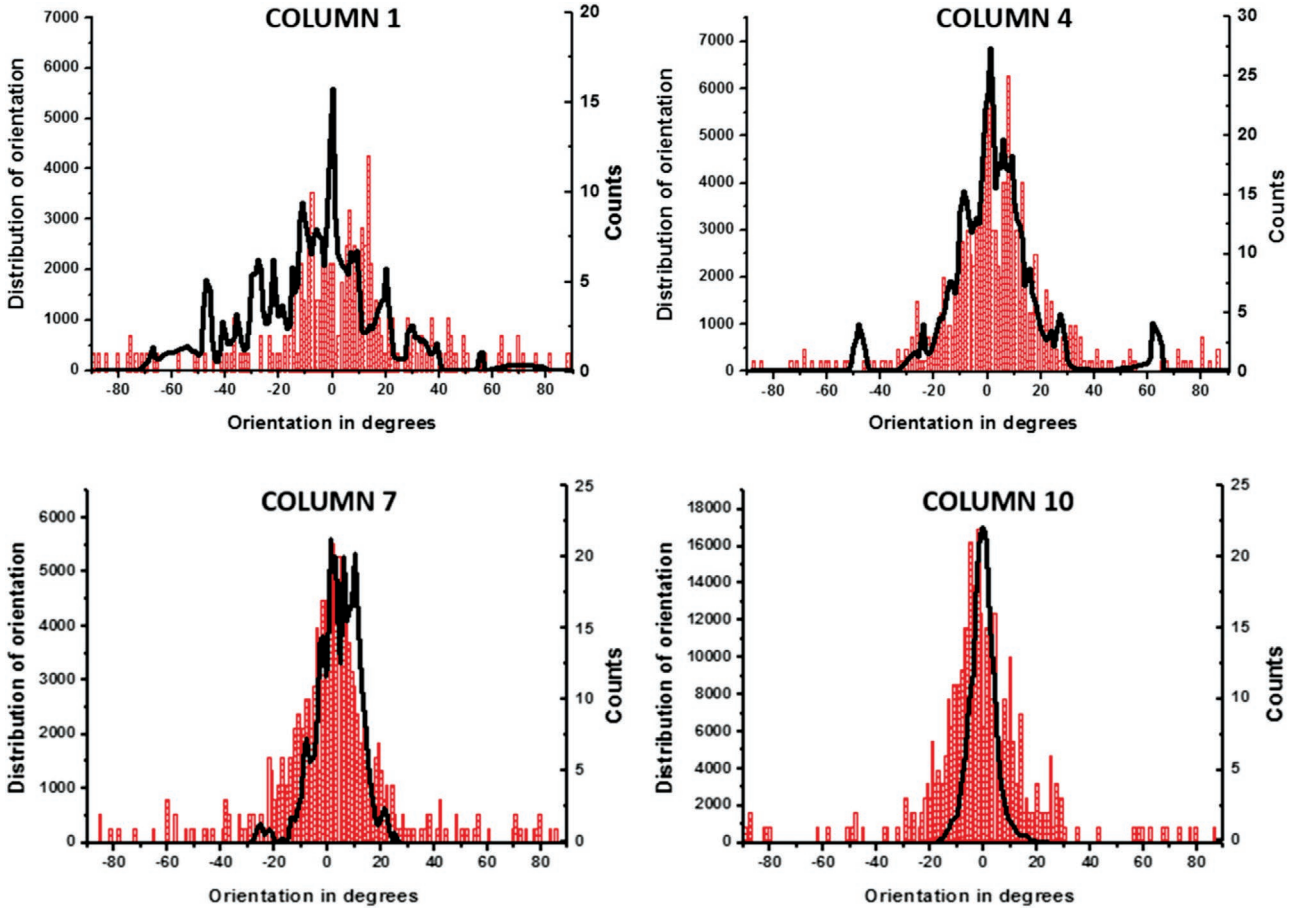

Figure 5. Comparative results of cell alignment measurements of both analysis methods are shown; for sake of simplicity, not all columns are shown (complete data can be seen in Figure S3, Supporting Information). Red columns represent results of CellProfiler analysis (Counts), whereas the black line shows cell alignment as determined by ImageJ analysis (Distribution of orientation).

3. Conclusion

In the pursuit of studying cell–material interactions in a unified fashion, it is pertinent that the developed systems are reproducible, accessible but also usable by others. In the development of high-throughput approaches for studying cell–material interactions, we found that the gradients we have developed in the past serve the purpose of these investigations. However, with new technology, there is the responsibility of allowing others to have either access to technology or be able to use it. Here, we successfully translated our topography gradient platform, which was somewhat difficult to use by non-experts, to a widely used and generic compatible well plate system. We succeeded to integrate our aligned gradient technology with conventional 96-well plates, without any leakages and keeping the surface topography intact. By integrating the gradient into the well plate, it is possible to perform a study involving four conditions in duplicate in one experiment rather than creating eight different gradient substrates that then may provide additional experimental errors. It allows, for example, to study various biological coating contributions of fibronectin, collagen, gelatin, or other biological stimulations in addition to topography alone in a single experiment. This translation included a careful upscaling of the gradient substrate dimension from a 1.0 × 1.0 cm to a 9.0 × 8.0 cm substrate to maximize the number of usable wells within the plate. We showed that integration of our technology with conventional cell culture methods for studying cell behavior does not alter or hamper the standardized protocols and allows for conventional handling in lab facilities at different locations. hBM-MSCs were able to grow inside the gradient topography well plates and the visualization could be performed on two completely different imaging setups without special modifications. As these results show promising implications for future development of universally applicable, high-throughput screening methods, we have also recognized that for the optimization and unification of data analysis, there are still some challenges within understanding cell–material interactions.

As shown in our study, there is a need to unify the data analysis approaches. Automated and manual data analysis methods still differ significantly from one another, as in this specific case came forward as the difference between analysis in two free-ware packages namely ImageJ and CellProfiler software. Careful consideration and refining of image-based cell-profiling methodologies will aid us in future biological discoveries.[60] Hence, in addition to unifying approaches to characterize

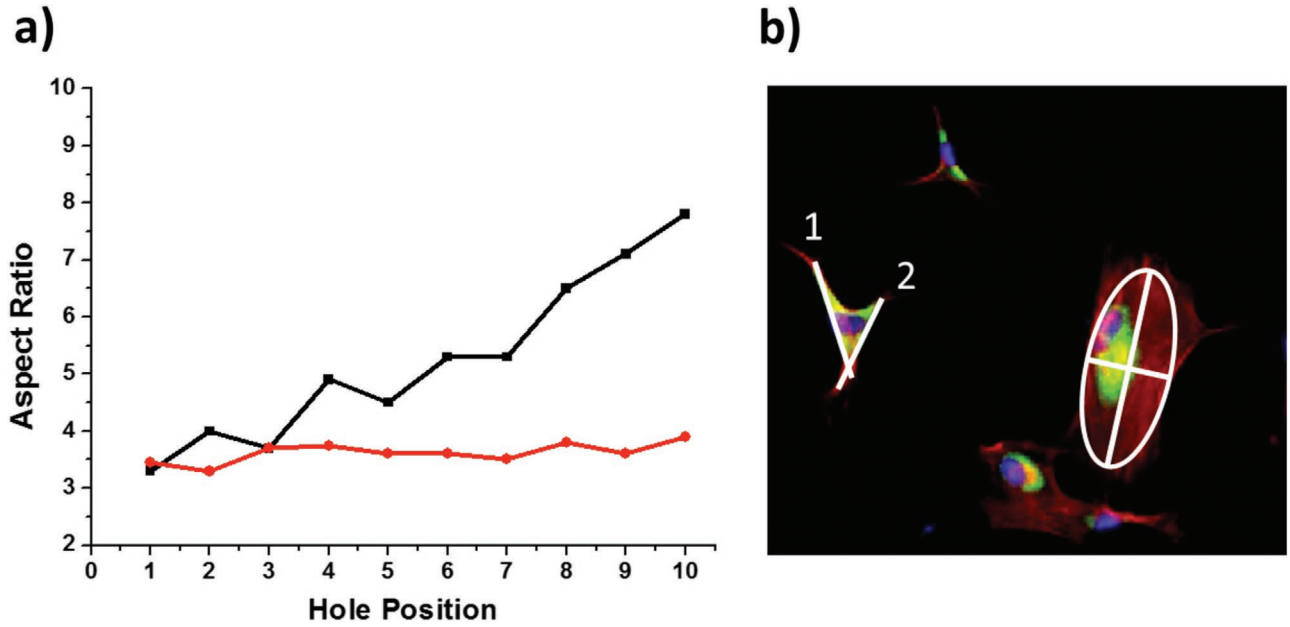

Figure 6. a) Comparative graphs of Aspect Ratio measurements in ImageJ (black) and CellProfiler software (red). A line connecting the dots serves as a guide to the eye. Both analyses show only slight deviation in cell aspect ratio in columns 1 through 6, after which an increase is observed by analysis in ImageJ software. b) Determination of the object's major and minor axis in CellProfiler software, and the corresponding ellipse formation (right). For more irregularly shaped cells, the program will calculate the axis based on the segmented region, which might be different from the axis determined manually. The calculated major axis may be axis 1 or axis 2, or even neither of them.

materials, the only real insights come from similarly unifying the data analysis approach. In our opinion, this discovery clearly emphasizes that the biointerface community has to adapt a more critical attitude toward observed cellular behavior as presented to us through our analysis systems.

4. Experimental Section

Materials: The PDMS was prepared using a Sylgard 184 elastomer kit obtained from Dow Corning (DowDuPont), according to their specifications. Greiner Bio-One no. 655101 bottomless 96-well plates served as the modifiable well plates.

AFM analysis was performed using a Catalyst Nanoscoop V (Bruker, Billerica, MA, USA), with NanoScoop Analysis (also Bruker) as analysis software. The AFM measurements were performed using Bruker model DNP-10 tip of non-conductive silicon nitride.

For visualization of the cells the Cell Painting protocol was followed, staining for nucleus (Hoechst 33342), endoplasmic reticulum (concavalin A, AlexaFluor488 conjugate), nucleoli (SYTO 14 green fluorescent nucleic acid stain), Golgi apparatus and plasma membrane (wheat germ agglutinin, AlexaFluor594 conjugate), F-actin (phalloidin AlexaFluor594 conjugate), and mitochondria (MitoTracker Deep Red). Stained cells were visualized using two different microscopy setups. A Nikon Eclipse TI series inverted epifluorescence microscope (indicated in Figure 4 as N-E) and a Zeiss AxioImager.Z1 fluorescence inverted microscope controlled by TissueFAXS software (Tissue-Gnostics GmbH, Vienna, Austria) were used, both at 10× magnification (air objective). Nikon NIS-Elements Viewer in combination with CellProfiler software, and TissueQuest in combination with ImageJ software were used for data analysis, respectively.

Polydimethylsiloxane Wrinkles: For the preparation of PDMS substrates, Silicone Elastomer Base and Silicone Curing Agent were used in a 10:1 weight ratio. After rigorous stirring and mixing, exactly 18 g of the mixture was poured in clean, squared, polystyrene Petri dishes (12 × 12 cm²) and left to degas at room temperature for 2 h under vacuum. After all gas bubbles had escaped, the petri dishes containing the mixture were cured overnight at 70 °C and ambient pressure. The cross-linked PDMS was removed from the petri dishes and cut into 9.0 × 10 cm² pieces and mounted on a custom-made stretching apparatus, applying uniaxial strain and stretching the substrate by 30% of its original length. A custom-made triangular mask with an angular aperture of 30° was put on top of the substrates (Figure 1), without using any chemical attachment or physical force enhancing the attachment. After doing so, the samples were treated with air plasma for 650 s at 25 mTorr of pressure. To ensure reproducibility, the stretched and covered PDMS substrates were placed inside the plasma oven (Diener Electronics ATTO) in the same orientation each time. After removal of the mask and relieving the stress, wrinkle formation occurred. All samples, including flat PDMS control substrates, received a post treatment of air plasma for 600 s at 150 mTorr to ensure complete oxidation and thereby creating a homogeneous surface chemical composition as well as surface stiffness making topography the only altering parameter.

Well Plate Embedding: Wrinkle gradient samples were cut into pieces of 95 × 75 mm, to meet the dimensions of wells A1-10 through H1-10 of a Greiner Bio-One no. 655101 96-well plate, sacrificing row 11 which served as a seam to connect the wrinkle gradient to row 12, which served as flat PDMS control (15 × 75 mm) (Figure S1, Supporting Information). After corrections were made to yield a good as possible, seamless fit with the bottom of the well plate; the latter was carefully covered with liquid PDMS using a syringe, in order to cover all the area surrounding the wells on the bottom side of the plate. Approximately 1.50 g of liquid PDMS per plate was used and plates were put to cure at 70° for 8–9 min for the liquid PDMS to transit into a stickier, glue-like state. This short pre-curing ensured a good bonding of PDMS substrates with the plate and hampers the "glue" from spilling into the wells and at the same time produces a liquid-tight connection preventing leakage and possible inter-well communications. The two pre-cut PDMS substrates (wrinkle gradient and flat control) were carefully positioned in the desired orientation on top of the glue and pressed carefully, though firmly to ensure a good well plate bottom connection. A second, empty well plate was put on top of the newly placed bottom and again a gripping force was applied, distributed evenly over the whole plate. After carefully

disassembling the "well plate sandwich," the connection was checked and enhanced by pressing each intersection with the tip of a pen, to guarantee the liquid-tight sealing of each well. After this, the plates were put to incubate at 70 °C for 20 min for the glue to harden and tightly connect the bottom to the plate. An extra well plate, together with a 4.5 kg weight were placed on top of the newly synthesized plates, applying evenly distributed pressure while plates cured. After curing, all wells were checked for inter-well communication by pipetting demi-water up and down in each well. If the water in a neighboring well responded to the pipetting, it meant inter-well communication was present. Plates deemed good were taken to the final step of the embedding process. Finally, to ensure a properly fixated bottom and to seal off the seam between the two PDMS substrates, approximately 30 g of liquid PDMS mixture was poured on top of the newly attached bottoms. Samples were put to cure at 70 °C and ambient pressure for 3 h ensuring a solid, sealed bottom. All wells were then washed twice with 200 µL PBS and plates were sealed with a lid to be stored for cell seeding.

Cell Culture and Seeding: After wells were washed with ethanol 70% twice and sterilized under UV light for 15 min, hBM-MSCs in fetal bovine serum p3 were seeded in the wells (100 µL) at a calculated density of 360×10^3 cells per milliliter. Samples were put to incubate overnight at 37 °C and 5% CO_2 saturation. After incubation, fenbendazol, a positive control yielding giant multi-nucleated cells (easily assessed during analysis) was added to wells G12 and H12; 25 µL solution of fenbendazol in DMSO, diluted 500 times (stock 3,34 mM). The multi-nucleated cells give a strong DAPI signal, as well as serve as a positive control for the DAPI staining. Samples were incubated overnight at the same conditions as mentioned above. The use of ethanol 70% in the specified amount of time does not affect the wrinkle features (Figure S5, Supporting Information), and deviations can be attributed to natural deviations in measurements, as well as between samples (Figure 2b).

Cell Adhesion Studies: Cells were stained for analysis by the two microscopy set-ups according to the Cell Painting protocol (Broad Institute).[59] A total of 100 µL (1 µM) of MitoTracker Deep Red FM was added to all wells and incubated at room temperature for 30 min, after which the cells were fixed using 4% paraformaldehyde and put to incubate in the dark at room temperature for 20 min. All wells were washed 3 times with 100 µL of GIBCO HBSS. After removal of HBSS, cells were permeabilized with 0.1% Triton X-100 (100 µL), after which samples were left at room temperature, in the dark for 10 min. All wells were washed again 3 times with HBSS and left in the dark at room temperature while the Cell Painting solution was prepared in HBSS, according to Broad Institute protocol. A total amount of 50 µL of the Cell Painting solution was added to each of the wells, after which the samples were left to incubate in the dark at room temperature for 30 min. Finally, the Cell Painting solution was removed and all wells were washed 3 times with 200 µL HBSS and stored in 200 µL HBSS in the dark at 4 °C, until imaging could commence.

Statistical Analysis: All data on wrinkle features is expressed as mean ± standard deviation of at least three samples. One-way analysis of variance, in combination with Tukey's post hoc test were performed to determine statistical significance (significant when $p < 0.05$) of data on well plate embedding (before and after, Figure S2, Supporting Information), using Origin 9.0 software package.

Supporting Information

Supporting Information is available from the Wiley Online Library or from the author.

Acknowledgements

The authors are very grateful for the financial support of the China Scholarship Council (nos. 201406630003 and 201608310113), the UMCG Microscopy and Imaging Center (UMIC) (NWO-grant 40-00506-98-9021), the Scientific Research Foundation of Qingdao University (Grant no. DC1900009689), and the Natural Science Foundation of Shandong Province, China (Grant no. ZR2019QC007).

Conflict of Interest

P.v.R. also is co-founder, scientific advisor, and share-holder of BiomACS BV, a biomedical oriented screening company.

Keywords

biointerfaces, gradients, high-throughput screening, stem cells, surface topography

Received: September 6, 2019
Revised: October 2, 2019
Published online: November 4, 2019

[1] A. S. Hayward, N. R. Cameron, S. A. Przyborski, in *Biointerfaces: Where Material Meets Biology* (Eds: D. W. Hutmacher, W. Chrzanwski), Royal Society of Chemistry, London **2014**.
[2] Y. Li, Y. Xiao, C. Liu, *Chem. Rev.* **2017**, *117*, 4376.
[3] R. Ogaki, M. Alexander, P. Kingshott, *Mater. Today* **2010**, *13*, 22.
[4] J. M. Anderson, *Semin. Immunol.* **2008**, *20*, 86.
[5] J. Li, *J. Nanomed. Res.* **2017**, *5*, 135.
[6] R. Ayala, C. Zhang, D. Yang, Y. Hwang, A. Aung, S. S. Shroff, F. T. Arce, R. Lal, G. Arya, S. Varghese, *Biomaterials* **2011**, *32*, 3700.
[7] K. S. Jones, *Semin. Immunol.* **2008**, *20*, 130.
[8] G. Huang, F. Li, X. Zhao, Y. Ma, Y. Li, M. Lin, G. Jin, T. J. Lu, G. M. Genin, F. Xu, *Chem. Rev.* **2017**, *117*, 12764.
[9] F. Gattazzo, A. Urciuolo, P. Bonaldo, *Biochim. Biophys. Acta, Gen. Subj.* **2014**, *1840*, 2506.
[10] S. D. Subramony, B. R. Dargis, M. Castillo, E. U. Azeloglu, M. S. Tracey, A. Su, H. H. Lu, *Biomaterials* **2013**, *34*, 1942.
[11] K. Kolind, K. W. Leong, F. Besenbacher, M. Foss, *Biomaterials* **2012**, *33*, 6626.
[12] S. Zijl, A. S. Vasilevich, P. Viswanathan, A. L. Helling, N. R. M. Beijer, G. Walko, C. Chiappini, J. de Boer, F. M. Watt, *Acta Biomater.* **2019**, *84*, 133.
[13] R. K. Das, O. F. Zouani, *Biomaterials* **2014**, *35*, 5278.
[14] D. E. Discher, P. Janmey, Y.-L. Wang, *Science* **2005**, *310*, 1139.
[15] A. Curtis, C. Wilkinson, *Biomaterials* **1997**, *18*, 1573.
[16] C. J. Bettinger, R. Langer, J. T. Borenstein, *Angew. Chem., Int. Ed.* **2009**, *48*, 5406.
[17] G. Abagnale, M. Steger, V. H. Nguyen, N. Hersch, A. Sechi, S. Joussen, B. Denecke, R. Merkel, B. Hoffmann, A. Dreser, U. Schnakenberg, A. Gillner, W. Wagner, *Biomaterials* **2015**, *61*, 316.
[18] J. Yang, F. R. A. J. Rose, N. Gadegaard, M. R. Alexander, *Adv. Mater.* **2009**, *21*, 300.
[19] M. M. Stevens, *Science* **2005**, *310*, 1135.
[20] A. M. Schaap-Oziemlak, P. T. Kühn, T. G. van Kooten, P. van Rijn, *RSC Adv.* **2014**, *4*, 53307.
[21] A. Higuchi, Q.-D. Ling, Y. Chang, S.-T. Hsu, A. Umezawa, *Chem. Rev.* **2013**, *113*, 3297.
[22] D. P. Dowling, I. S. Miller, M. Ardhaoui, W. M. Gallagher, *J. Biomater. Appl.* **2011**, *26*, 327.
[23] R. J. Narayan, *Philos. Trans. R. Soc., A* **2010**, *368*, 1831.
[24] L. L. Hench, J. M. Polak, *Science* **2002**, *295*, 1014.
[25] R. Langer, D. A. Tirrell, *Nature* **2004**, *428*, 487.
[26] V. Vogel, M. Sheetz, *Nat. Rev. Mol. Cell Biol.* **2006**, *7*, 265.

[27] B. Geiger, J. P. Spatz, A. D. Bershadsky, *Nat. Rev. Mol. Cell Biol.* **2009**, *10*, 21.
[28] C. C. Dufort, M. J. Paszek, V. M. Weaver, *Nat. Rev. Mol. Cell Biol.* **2011**, *12*, 308.
[29] O. Chaudhuri, L. Gu, D. Klumpers, M. Darnell, S. A. Bencherif, J. C. Weaver, N. Huebsch, H. P. Lee, E. Lippens, G. N. Duda, D. J. Mooney, *Nat. Mater.* **2016**, *15*, 326.
[30] S. Khetan, M. Guvendiren, W. R. Legant, D. M. Cohen, C. S. Chen, J. A. Burdick, *Nat. Mater.* **2013**, *12*, 458.
[31] S. Dupont, L. Morsut, M. Aragona, E. Enzo, S. Giulitti, M. Cordenonsi, F. Zanconato, J. Le Digabel, M. Forcato, S. Bicciato, N. Elvassore, S. Piccolo, *Nature* **2011**, *474*, 179.
[32] L. Dong, K. Cheng, Y. Zhou, M. Yu, J. Gong, Y. Lin, Q. Luo, Q. Wang, W. Weng, H. Wang, *ACS Appl. Mater. Interfaces* **2017**, *9*, 15274.
[33] P. Wang, D. T. Bennetsen, M. Foss, H. Thissen, P. Kingshott, *Biointerphases* **2015**, *10*, 04A306.
[34] T. Lecuit, P.-F. Lenne, *Nat. Rev. Mol. Cell Biol.* **2007**, *8*, 633.
[35] T. Yeung, P. C. Georges, L. A. Flanagan, B. Marg, M. Ortiz, M. Funaki, N. Zahir, W. Ming, V. Weaver, P. A. Janmey, *Cell Motil. Cytoskeleton* **2005**, *60*, 24.
[36] M. A. Bucaro, Y. Vasquez, B. D. Hatton, J. Aizenberg, *ACS Nano* **2012**, *6*, 6222.
[37] C. C. Barrias, M. C. L. Martins, G. Almeida-Porada, M. A. Barbosa, P. L. Granja, *Biomaterials* **2009**, *30*, 307.
[38] J. Kim, H. N. Kim, K. T. Lim, Y. Kim, S. Pandey, P. Garg, Y. H. Choung, P. H. Choung, K. Y. Suh, J. H. Chung, *Biomaterials* **2013**, *34*, 7257.
[39] J. Wu, Z. Mao, H. Tan, L. Han, T. Ren, C. Gao, *Interface Focus* **2012**, *2*, 337.
[40] P. T. Kühn, Q. Zhou, T. A. B. van der Boon, A. M. Schaap-Oziemlak, T. G. van Kooten, P. van Rijn, *ChemNanoMat* **2016**, *2*, 407.
[41] Q. Zhou, P. T. Kühn, T. Huisman, E. Nieboer, C. van Zwol, T. G. van Kooten, P. van Rijn, *Sci. Rep.* **2015**, *5*, 16240.
[42] Q. Zhou, O. Castañeda Ocampo, C. F. Guimarães, P. T. Kühn, T. G. Van Kooten, P. Van Rijn, *ACS Appl. Mater. Interfaces* **2017**, *9*, 31433.
[43] Q. Zhou, L. Ge, C. F. Guimarães, P. T. Kühn, L. Yang, P. van Rijn, *Adv. Mater. Interfaces* **2018**, *1800504*, 4.
[44] L. Smith Callahan, *High-Throughput* **2018**, *7*, 1.
[45] A. L. Hook, D. G. Anderson, R. Langer, P. Williams, M. C. Davies, M. R. Alexander, *Biomaterials* **2010**, *31*, 187.
[46] A. Buxboim, K. Rajagopal, A. E. X. Brown, D. E. Discher, *J. Phys.: Condens. Matter* **2010**, *22*, 194116.
[47] J. Genzer, *Annu. Rev. Mater. Res.* **2012**, *42*, 435.
[48] M. Whang, J. Kim, *Tissue Eng. Regener. Med.* **2016**, *13*, 126.
[49] P. Y. Wang, L. R. Clements, H. Thissen, S. C. Hung, N. C. Cheng, W. B. Tsai, N. H. Voelcker, *RSC Adv.* **2012**, *2*, 12857.
[50] M. Hulsman, F. Hulshof, H. Unadkat, B. J. Papenburg, D. F. Stamatialis, R. Truckenmüller, C. Van Blitterswijk, J. De Boer, M. J. T. Reinders, *Acta Biomater.* **2015**, *15*, 29.
[51] A. A. K. Moe, M. Suryana, G. Marcy, S. K. Lim, S. Ankam, J. Z. W. Goh, J. Jin, B. K. K. Teo, J. B. K. Law, H. Y. Low, E. L. K. Goh, M. P. Sheetz, E. K. F. Yim, *Small* **2012**, *8*, 3050.
[52] J. Lovmand, J. Justesen, M. Foss, R. H. Lauridsen, M. Lovmand, C. Modin, F. Besenbacher, F. S. Pedersen, M. Duch, *Biomaterials* **2009**, *30*, 2015.
[53] S. An, J. Lim, D. Choi, H. Hong, H. W. Kim, S. M. Park, J. W. Rhie, D. S. Kim, *Microelectron. Eng.* **2017**, *174*, 28.
[54] J. Hu, A. A. Gondarenko, A. P. Dang, K. T. Bashour, R. S. O'Connor, S. Lee, A. Liapis, S. Ghassemi, M. C. Milone, M. P. Sheetz, M. L. Dustin, L. C. Kam, J. C. Hone, *Nano Lett.* **2016**, *16*, 2198.
[55] H. V. Unadkat, M. Hulsman, K. Cornelissen, B. J. Papenburg, R. K. Truckenmuller, A. E. Carpenter, M. Wessling, G. F. Post, M. Uetz, M. J. T. Reinders, D. Stamatialis, C. A. van Blitterswijk, J. de Boer, *Proc. Natl. Acad. Sci. U. S. A.* **2011**, *108*, 16565.
[56] G. R. Liguori, Q. Zhou, T. Tavares, A. Liguori, G. G. Barros, P. T. Kühn, L. Felipe, P. Moreira, P. Van Rijn, M. C. Harmsen, **2019**, *2019*, 5387850.
[57] N. R. M. Beijer, A. S. Vasilevich, B. Pilavci, R. K. Truckenmüller, Y. Zhao, S. Singh, B. J. Papenburg, J. De Boer, *Adv. Biosyst.* **2017**, *1*, 1700002.
[58] S. Watari, K. Hayashi, J. A. Wood, P. Russell, P. F. Nealey, C. J. Murphy, D. C. Genetos, *Biomaterials* **2012**, *33*, 128.
[59] M. A. Bray, S. Singh, H. Han, C. T. Davis, B. Borgeson, C. Hartland, M. Kost-Alimova, S. M. Gustafsdottir, C. C. Gibson, A. E. Carpenter, *Nat. Protoc.* **2016**, *11*, 1757.
[60] J. C. Caicedo, S. Cooper, F. Heigwer, S. Warchal, P. Qiu, C. Molnar, A. S. Vasilevich, J. D. Barry, H. S. Bansal, O. Kraus, M. Wawer, L. Paavolainen, M. D. Herrmann, M. Rohban, J. Hung, H. Hennig, J. Concannon, I. Smith, P. A. Clemons, S. Singh, P. Rees, P. Horvath, R. G. Linington, A. E. Carpenter, *Nat. Methods* **2017**, *14*, 849.